Reciprocal allostery arising from a bienzyme assembly controls aromatic amino acid biosynthesis in *Prevotella nigrescens*

Received for publication, March 28, 2021, and in revised form, July 28, 2021 Published, Papers in Press, July 31, 2021,
https://doi.org/10.1016/j.jbc.2021.101038

Yu Bai and Emily J. Parker*

From the Maurice Wilkins Centre, Ferrier Research Institute, Victoria University of Wellington, Wellington, New Zealand

Edited by Wolfgang Peti

Modular protein assembly has been widely reported as a mechanism for constructing allosteric machinery. Recently, a distinctive allosteric system has been identified in a bienzyme assembly comprising a 3-deoxy-D-*arabino* heptulosonate-7-phosphate synthase (DAH7PS) and chorismate mutase (CM). These enzymes catalyze the first and branch point reactions of aromatic amino acid biosynthesis in the bacterium *Prevotella nigrescens* (*Pni*DAH7PS), respectively. The interactions between these two distinct catalytic domains support functional interreliance within this bifunctional enzyme. The binding of prephenate, the product of CM-catalyzed reaction, to the CM domain is associated with a striking rearrangement of overall protein conformation that alters the interdomain interactions and allosterically inhibits the DAH7PS activity. Here, we have further investigated the complex allosteric communication demonstrated by this bifunctional enzyme. We observed allosteric activation of CM activity in the presence of all DAH7PS substrates. Using small-angle X-ray scattering (SAXS) experiments, we show that changes in overall protein conformations and dynamics are associated with the presence of different DAH7PS substrates and the allosteric inhibitor prephenate. Furthermore, we have identified an extended interhelix loop located in CM domain, loop$_{C320\text{-}F333}$, as a crucial segment for the interdomain structural and catalytic communications. Our results suggest that the dual-function enzyme *Pni*DAH7PS contains a reciprocal allosteric system between the two enzymatic moieties as a result of this bidirectional interdomain communication. This arrangement allows for a complex feedback and feedforward system for control of pathway flux by connecting the initiation and branch point of aromatic amino acid biosynthesis.

Allostery is generally defined as the modulation of protein function that arises from ligand binding at a remote site (1, 2). Multidomain protein assemblies have been demonstrated as an effective means of delivering allosteric functionality (3–5). Allostery plays an important role in many biosynthetic pathways, where key enzymes are allosterically controlled by pathway end products or intermediates. In some cases, key regulatory enzymes have recruited extra structural elements to the core catalytic unit to acquire allosteric control in response to metabolite concentrations (6–8). Generally, the recruited regulatory elements accommodate effector binding sites and initiate the allosteric signal transduction, delivering activity modulation at the active site (9–13).

Modular assemblies for the delivery of allostery have been well studied in 3-deoxy-D-*arabino*-heptulosonate 7-phosphate synthase (DAH7PS). DAH7PS initiates the shikimate pathway for the biosynthesis of aromatic amino acids (Phe, Tyr, and Trp), by catalyzing the reaction between phosphoenolpyruvate (PEP) and erythrose 4-phosphate (E4P) to produce DAH7P. This reaction is dependent on the presence of a divalent metal ion, such as Mn^{2+}, Cd^{2+}, and Zn^{2+} (14, 15). Allosteric regulation of this gateway enzyme tunes the output of the shikimate pathway to cellular requirements (6–8). DAH7PS typically exists as a homotetramer or homodimer of catalytic subunits that comprise a $(\beta/\alpha)_8$ TIM barrel (11, 16–20). The acquisition of allostery by the DAH7PS enzyme family involves diverse additions to the core barrel (21), among which the adornments of discrete structural modules to either end of the DAH7PS domain are observed in one subtype of DAH7PS enzymes (type Iβ). The allosteric response conferred by these allosteric modules is characterized by dramatic conformational changes in response to allosteric ligand binding (11, 18). In addition to protein modules that solely deliver allostery, type Iβ DAH7PS proteins are also observed to be covalently linked, due to gene fusion, to another enzyme in aromatic amino acid biosynthesis—chorismate mutase (CM) (10, 11, 22).

CM is a pivotal enzyme at a branch point of the shikimate pathway, catalyzing the transformation of chorismate to prephenate, which ultimately delivers Phe and Tyr. Two main classes of CM enzymes have been identified (23, 24). The CM enzymes associated with DAH7PS belong to the AroQ subtype and exert function as a homodimer of three-helix bundles (25). The AroQ CM is fused to either the N-terminus or C-terminus of DAH7PS. For the N-terminal CM-linked DAH7PS enzymes, such as the DAH7PS from *Bacillus subtilis* (*Bsu*DAH7PS), *Listeria monocytogenes* (*Lmo*DAH7PS), and *Geobacillus* sp. (*Gsp*DAH7PS), the role of CM as an allosteric domain is well demonstrated (10, 11, 22). The crystal structure of *Gsp*DAH7PS shows that the N-terminal CM of each DAH7PS barrel pairs

* For correspondence: Emily J. Parker, emily.parker@vuw.ac.nz.

with its diagonally opposed counterpart and forms a dimer at either side of the DAH7PS tetrameric core (Fig. 1, *A*) (11). The binding of prephenate (or chorismate) to the active site of CM is associated with a conformational rearrangement where the CM dimers shift toward a tighter association with the tetrameric DAH7PS core. This significant conformational change results in the occlusion of the entrances of DAH7PS active sites and disrupts catalysis (Fig. 1, *A*) (11). In this complex system, although the CM is catalytically functional, it appears to work as nothing more than a regulatory module to provide a gating mechanism and the CM active site acts as an allosteric effector binding site. In addition to the AroQ CM, a monofunctional unregulated CM belonging to AroH subtype is encoded in the organisms with N-terminal CM-linked DAH7PS. This AroH CM exhibits a higher enzymatic activity and is predicted to be the main *in vivo* catalyst for the production of prephenate (26).

In contrast, the C-terminal CM-linked DAH7PS is often found as the only source of CM activity in the organisms where it is identified from according to classification of CM enzymes retrieved from Pfam database (27). Compared with other well-studied DAH7PS proteins, these enzymes adopt distinctive machinery for the delivery of both allostery and catalysis, as reported by our recent study on a DAH7PS from *Prevotella nigrescens* (*Pni*DAH7PS) (15). *Pni*DAH7PS is a bifunctional enzyme consisting of an N-terminal DAH7PS and a C-terminal CM domain, and separation of the two domains results in a dramatic attenuation of both enzymatic activities. The structural investigation into this protein revealed that it displays a unique homodimeric assembly with dimerization of the helical CM domains and no direct contact between DAH7PS barrels (15). Moreover, DAH7PS activity is allosterically inhibited by prephenate (15). This allosteric inhibition is accompanied by a striking conformational change that alters the interdomain interactions between DAH7PS and CM (15), which indicates that a manipulation of the interdomain interaction is the mechanism underpinning allosteric inhibition.

A similar functional reliance between the DAH7PS and CM is observed in the noncovalent DAH7PS-CM complex found in *Corynebacterium glutamicum* (*Cgl*DAH7PS-CM) (28) and *Mycobacterium tuberculosis* (*Mtu*DAH7PS-CM) (29). In the *Mtu*DAH7PS-CM complex, CM is activated upon complexation with DAH7PS and inhibited by the binding of allosteric inhibitors, Tyr and Phe, at allosteric binding sites within each DAH7PS subunit (30–32). The structure of the *Mtu*DAH7PS-CM complex showed that the DAH7PS and CM subunits interact with each other extensively and form a stable interface (Fig. 1, *B*) (29, 31). Molecular dynamics simulations suggest that the interface between DAH7PS and CM subunits is noticeably more flexible when the inhibitors are bound, which may result in a less stable DAH7PS-CM interaction (33), suggesting a crucial role of this stable interface for delivering CM function.

In contrast to the *Mtu*DAH7PS-CM complex, the functional enhancements that arise from association are mutual between DAH7PS and CM activities of *Pni*DAH7PS, which suggests an extensive DAH7PS-CM interaction and communication pathway between the two functional domains. Furthermore, SAXS data of ligand-free *Pni*DAH7PS showed that it is highly flexible and able to adopt a broad range of relative domain conformations (15), indicating a lack of stable domain interface, unlike *Mtu*DAH7PS-CM. How then does such a flexible structure of *Pni*DAH7PS deliver the functional communication between two active sites? To address this question, we conducted a series of biochemical and structural investigations on *Pni*DAH7PS in the presence of different ligands. Our studies reveal that dynamic and variable interdomain interactions for *Pni*DAH7PS are associated with the DAH7PS-catalyzed reaction and that these result in reciprocal allosteric regulation between the DAH7PS and CM active sites.

Results

DAH7PS allosterically activates CM

Previous kinetic studies revealed the interdependency of the DAH7PS and CM catalytic functions of *Pni*DAH7PS and demonstrated that prephenate binding to the CM domain allosterically inhibits DAH7PS activity (15). To understand the domain interdependency and the full allosteric functionality of

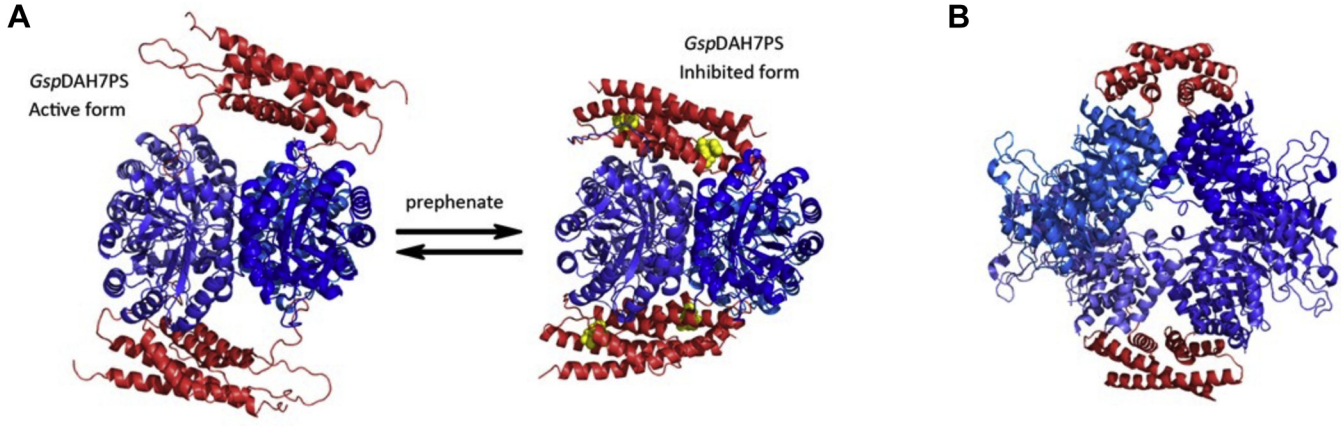

Figure 1. Crystal structures and homology model illustrating the allosteric regulations of *Gsp*DAH7PS and the architecture of *Mtu*DAH7PS-CM complex. DAH7PS barrels are shown in *blue*, and CM domains are colored in *red*. *A*, the binding of prephenate (*yellow spheres*) shifts the conformational population of *Gsp*DAH7PS resulting in inhibition of DAH7PS activity (11). *B*, noncovalent complex between *Mtu*DAH7PS and the intracellular *Mtu*CM (31).

this protein, we investigated the effect of substrate binding and catalysis in the DAH7PS active site on the catalysis of the CM reaction. The catalytic rate for the CM reaction was measured directly in the presence of the components of DAH7PS-catalyzed reaction at saturating concentrations, either individually or in combination, or in the presence of the reaction products, DAH7P and phosphate (Fig. 2). Interestingly, we observed a greater than twofold increase in the rate of chorismate consumption only in the presence of all DAH7PS reaction components (PEP/Mn^{2+}/E4P, Fig. 2, *A*). It should be noted that under this experimental condition, catalysis was occurring simultaneously at both CM and DAH7PS active sites, and the enzyme comprised various populations complexed with substrates or intermediates or products. The presence of either an incomplete set of DAH7PS reaction components or a high concentration of the product mixture (DAH7P and phosphate) altered CM activity insignificantly (Fig. 2, *A*). This observation implies that there is an allosteric activation effect, exerted by the occupancy and catalysis at the DAH7PS active site, on the CM catalytic function for *Pni*DAH7PS. Furthermore, the DAH7P/phosphate combination at high concentrations competitively inhibited the DAH7PS reaction (Fig. S1). Therefore, DAH7PS active site occupancy alone is insufficient to elicit the allosteric activation.

In contrast, when the same analysis was carried out for the N-terminal CM-linked *Gsp*DAH7PS, no variation in the CM reaction rate was detected with any combination of the DAH7PS substrates (Fig. 2, *B*). This finding indicates that the observed allosteric activation of CM activity by binding and/or catalytic events at the DAH7PS reaction is specific to *Pni*DAH7PS.

Conformational changes of Pni*DAH7PS are related to the occupancy of the DAH7PS active site*

The structural effects of DAH7PS substrates on *Pni*DAH7PS were inspected using SAXS. These measurements were achieved by passing the enzyme through a size exclusion column, using an elution buffer containing combinations of PEP, E4P, and $MnSO_4$, prior to exposure to the X-ray beam. The scattering profile from this protein is denoted here as *Pni*DAH7PS_{rxn}. With all three reaction components present, the protein displays a more compact structure, compared with that of the ligand-free enzyme, as evidenced by the reduced R_g, D_{max}, and V_p values (Table 1). Furthermore, the Kratky and Porod–Debye plots derived from the scattering data indicate a decreased flexibility in the protein (Fig. 3, *C*). It should be noted that, given that the DAH7PS-catalyzed reaction is underway in the presence of both substrates and metal ion (PEP, E4P, and Mn^{2+}), the SAXS scattering of *Pni*DAH7PS_{rxn} arises from the average conformation of the protein through the catalytic cycle.

Further SAXS analysis revealed that the addition of both PEP and Mn^{2+} also alters the scattering from the protein, implying that this liganded *Pni*DAH7PS (*Pni*DAH7PS_{PM}) adopts a more compact structure than the ligand-free protein, albeit not as compressed as that of the protein in the presence of all DAH7PS reaction components (Table 1 and Fig. 3, *B*). In addition to reductions of R_g and D_{max} values, structural rigidification was also observed, as indicated by the Kratky and Porod–Debye transformations (Fig. 3, *C* and *D*).

To visualize the conformational changes indicated by the scattering profiles described above, rigid body modeling was carried out using models for *Pni*DAH7PS^D and *Pni*DAH7PS^{CM} (15) and the real space information extracted from the SAXS data. Rigid body models for ligand-free *Pni*DAH7PS, *Pni*DAH7PS_{PM}, and *Pni*DAH7PS_{rxn} yield reasonable fits (χ^2 = 0.3, 1.47, and 1.43, respectively) to their corresponding experimental SAXS data (Fig. 4). Both the models of *Pni*DAH7PS_{PM} and *Pni*DAH7PS_{rxn} adopt more compact spatial organizations compared with that of ligand-free *Pni*DAH7PS (Fig. 4). It is of particular note that in the

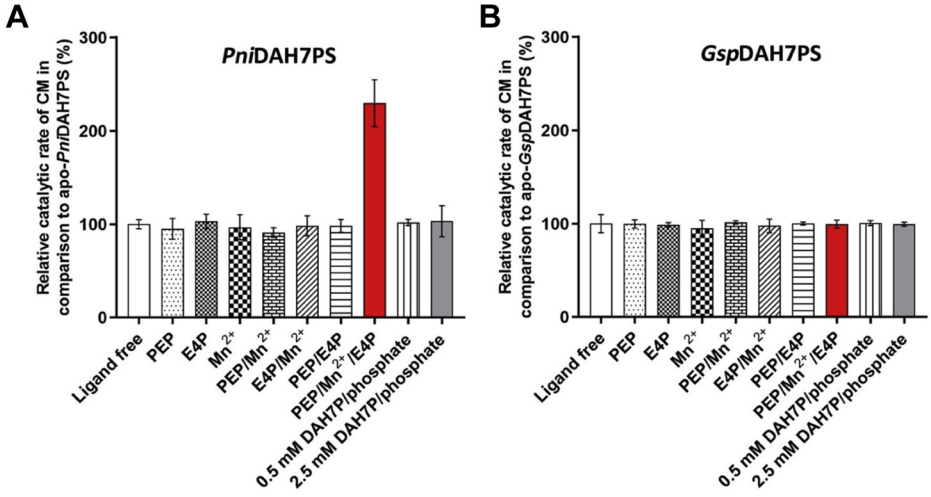

Figure 2. The presence of PEP, Mn^{2+}, and E4P boosts the CM catalytic rate of *Pni*DAH7PS. Error bars represent the standard deviation of triplicate measurements. The CM catalytic rates of *Pni*DAH7PS (*A*) and *Gsp*DAH7PS (*B*) were examined respectively in the presence of a variety of combinations of DAH7PS reaction substrates, product, and Mn^{2+} ion as indicated. Direct interference by the components of DAH7PS reaction in the detection of CM activity was excluded, as detailed in the Experimental procedures section.

Table 1
SAXS parameters of ligand-free *Pni*DAH7PS, *Pni*DAH7PS$_{PM}$, and *Pni*DAH7PS$_{rxn}$

	Ligands present		
	Ligand-free	PEP/Mn^{2+}	PEP/Mn^{2+}/E4P
Guinier analysis			
R_g (Å)	42.0 ± 1.2	39.4 ± 0.8	35.8 ±1.0
I(0) (cm^{-1})	0.08 ± 0.00	0.07 ± 0.00	0.07 ± 0.00
Correlation coefficient, R^2	0.99	0.99	0.99
Pairwise distribution analysis			
R_g (Å)	44.1 ± 0.2	41.0 ± 0.1	37.7 ± 0.6
I(0) (cm^{-1})	0.08 ± 0.00	0.07 ± 0.00	0.07 ± 0.00
D_{max} (Å)	152.3	142.7	140.2
V_p (nm^3)	137	139	121
MM_{porod}			
MM (kDa)	81	82	71
Number of subunits	2	2	2

Abbreviations: MM_{porod}, molecular mass estimated from Porod volume; V_p, Porod volume.
The uncertainties represent SDs estimated by the error propagation from the experimental data.

model for *Pni*DAH7PS$_{rxn}$ the two DAH7PS barrels are predicted to be positioned in close proximity to the CM dimer, as demonstrated by the decreased distance, from 39 Å to 27 Å, between residues R165 (NH1 atom) and R312 (NH1 atom) in the same chain, which are respectively situated at the centers of DAH7PS and CM active sites. This model might provide a structural rationale for forming an extensive interdomain interface and subsequently promoting both CM and DAH7PS activities under these conditions (Fig. 4, *C*). These SAXS-based observations and analysis suggest that a diverse range of interdomain interactions are possible and that conformational plasticity is associated with the DAH7PS catalytic cycle.

A loop truncation in the CM domain interferes with catalysis and conformation of Pni*DAH7PS*

A multisequence alignment (MSA) of a number of AroQ CM enzymes, including the independent monofunctional CM enzymes from *Pyrococcus furiosus* (*Pfu*CM) and *Aeropyrum pernix* (*Ape*CM), and the CM domains of *Pni*DAH7PS and the C-terminal CM-linked DAH7PS from *Porphyromonas gingivalis*, *Pgi*DAH7PS (*Pni*DAH7PS^{CM} and *Pgi*DAH7PS^{CM}), was constructed. This MSA and structural comparison revealed that in comparison to the discrete AroQ CM proteins, *Pni*DAH7PS^{CM} contains a ∼10 residue extension to the α2-α3 loop, loop$_{C320\text{-}F333}$ (Fig. 5). This loop extension is also observed in other CM domains linked to the C-terminal of a DAH7PS catalytic barrel.

To determine whether this extended loop affects the function and structure of *Pni*DAH7PS, a variant of *Pni*DAH7PS with a shortened loop (*Pni*DAH7PS$^{\Delta 5AA}$) was generated, by removing five residues (CGIDT) from the loop. The circular dichroism (CD) spectrum for *Pni*DAH7PS$^{\Delta 5AA}$ resembles that of wild-type enzyme, which implies that protein folding is not disrupted by the loop truncation (Fig. S2). Kinetic measurements of this variant demonstrated a considerable loss in the CM specificity constant, as evidenced by the decrease in the k_{cat}/K_M value for chorismate from 0.22 to 5.7 × 10^{-2} $\mu M^{-1}{\cdot}s^{-1}$ (Table 2). Notably, in addition to impaired CM catalysis, the DAH7PS activity of *Pni*DAH7PS$^{\Delta 5AA}$ was also significantly attenuated; the apparent specificity constant k_{cat}/K_m values for PEP and E4P were decreased respectively from 0.41 and 0.29 $\mu M^{-1}{\cdot}s^{-1}$ to 4.7 × 10^{-2} and 1.8 × 10^{-2} $\mu M^{-1}{\cdot}s^{-1}$ (Table 2).

In parallel, we examined the structural properties of *Pni*DAH7PS$^{\Delta 5AA}$ using SAXS experiments. The scattering data

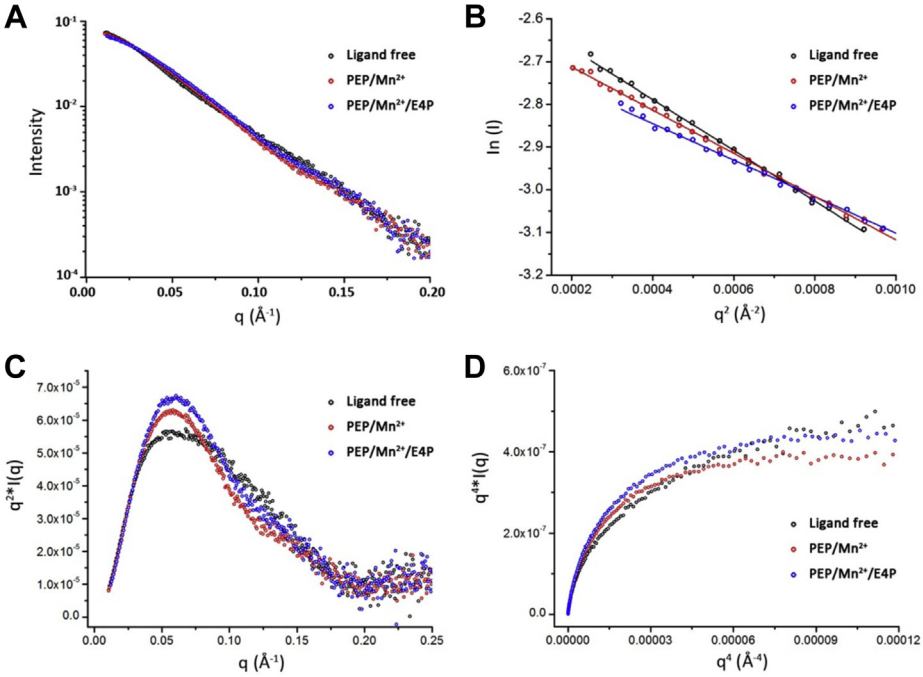

Figure 3. Analysis of the SAXS data of ligand-free *Pni*DAH7PS (*black*) and *Pni*DAH7PS$_{PM}$ (*red*) and *Pni*DAH7PS$_{rxn}$ (*blue*). *A*, SAXS profiles (log *I*(*q*) *versus q*). *B*, Guinier plots (ln *I*(*q*) *versus* q^2). *C*, Kratky plot (q^2**I*(*q*) *versus q*). *D*, Porod–Debye plot (q^4**I*(*q*) *versus* q^4) limited to the range of the SAXS data for which the Guinier linearity was observed.

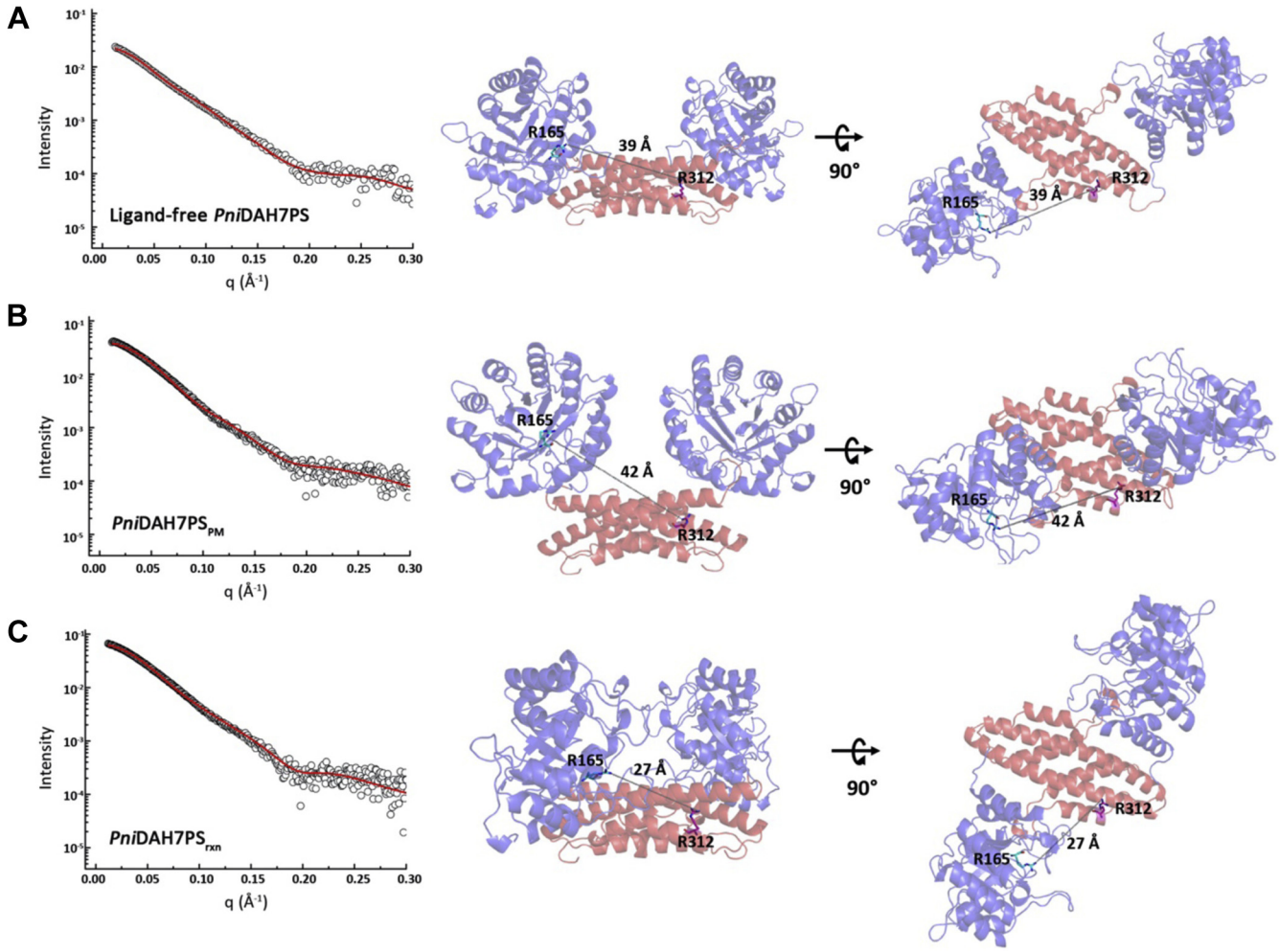

Figure 4. Rigid body models for ligand-free *Pni*DAH7PS, *Pni*DAH7PS$_{PM}$, and *Pni*DAH7PS$_{rxn}$ derived SAXS data. DAH7PS and CM domains are respectively colored *blue* and *red*, and the distances between the NH1 atom of R165 (*cyan stick*) and the NH1 atom of R312 (*pink stick*) are indicated as *gray dash lines*. *A*, rigid body model of ligand-free *Pni*DAH7PS and the fit to the experimental SAXS data (χ^2 = 0.3). *B*, rigid body model of *Pni*DAH7PS$_{PM}$ and the fit to the experimental SAXS data (χ^2=1.47). *C*, rigid body model of *Pni*DAH7PS$_{rxn}$ and the fit to the experimental SAXS data (χ^2 = 1.43).

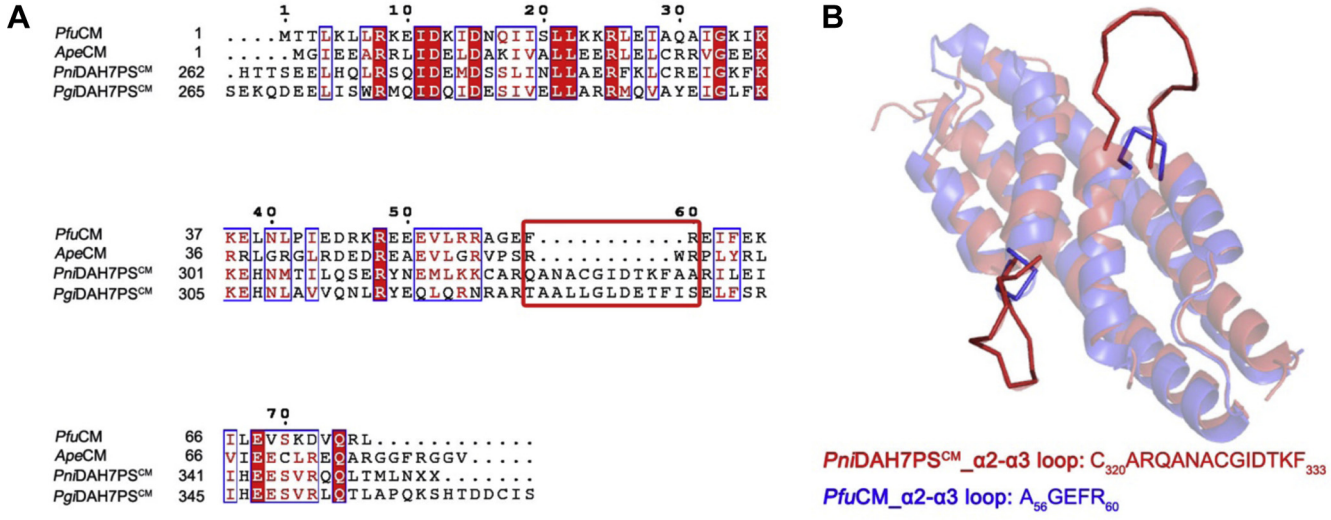

Figure 5. Sequence and structural alignments predict a loop extension within *Pni*DAH7PS^{CM}. *A*, the sequence alignment of *Pni*DAH7PS^{CM} with *Pgi*DAH7PS^{CM} with monofunctional AroQ CMs. The *red rectangle* highlights the unaligned region that is predicted to be an extended α2-α3 loop. *B*, the structural alignment between *Pfu*CM (crystal structure, shown in *blue cartoon*) and *Pni*DAH7PS^{CM} (homology model, shown in *red cartoon*), showing the extended loop between helices 2 and 3.

Table 2
Kinetic characteristics of the DAH7PS and CM functions of *Pni*DAH7PS$^{\Delta 5AA}$ and the kinetic parameters of *Pni*DAH7PS, *Pni*DAH7PS^{D}, and *Pni*DAH7PS^{CM} for comparison

Enzyme	DAH7PS activity					CM activity		
	K_M^{PEP} (μM)	K_M^{E4P} (μM)	k_{cat} (s^{-1})	k_{cat}/K_M^{PEP} ($\mu M^{-1}\cdot s^{-1}$)	k_{cat}/K_M^{E4P} ($\mu M^{-1}\cdot s^{-1}$)	K_M (μM)	k_{cat} (s^{-1})	k_{cat}/K_M ($\mu M^{-1}\cdot s^{-1}$)
*Pni*DAH7PS (15)	41 ± 4	58 ± 6	16.8 ± 0.5	0.41	0.29	7.6 ± 0.6	1.68 ± 0.06	0.22
*Pni*DAH7PS$^{\Delta 5AA}$	212 ± 51	556 ± 77	11 ± 1	4.7×10^{-2}	1.8×10^{-2}	21 ± 2	1.20 ± 0.02	5.7×10^{-2}
*Pni*DAH7PS^{D} (15)	262 ± 25	652 ± 60	1.6 ± 0.1	6.1×10^{-3}	2.5×10^{-3}	ND	ND	ND
*Pni*DAH7PS^{CM} (15)	ND	ND	ND	ND	ND	84 ± 5	2.01 ± 0.07	2.4×10^{-2}

Abbreviations: ND, not detectable; *Pni*DAH7PS^{D}, DAH7PS domain variant of *Pni*DAH7PS; *Pni*DAH7PS^{CM}, CM domain variant of *Pni*DAH7PS.
The Michaelis constants for the DAH7PS activity were obtained via fitting kinetic data to the equation of Alberty (as detailed in the Experimental procedures section). The uncertainty values represent the SD from triplicate measurements.

reveals that ligand-free *Pni*DAH7PS$^{\Delta 5AA}$ retains a flexible and elongated homodimeric structure (Table 3). However, the increased R_g and V_p values of ligand-free *Pni*DAH7PS$^{\Delta 5AA}$ (Table 3), compared with those for wild-type ligand-free *Pni*-DAH7PS, indicate that the loop truncation increased the average size of the *Pni*DAH7PS homodimer (Fig. 6, *D*). Following the addition of PEP and Mn^{2+}, the conformation of *Pni*DAH7PS$^{\Delta 5AA}$ (*Pni*DAH7PS$_{PM}^{\Delta 5AA}$) became more compact, presenting a similar average size to that of *Pni*DAH7PS$_{PM}$ (Table 3). Whereas the Kratky and Porod–Debye transformations of *Pni*DAH7PS$_{PM}^{\Delta 5AA}$ showed considerable flexibility, which differs from the rigidification of the wild-type protein upon the binding of PEP and Mn^{2+} (Fig. 6, *H* and *I*). Furthermore, with the presence of PEP/Mn^{2+}/E4P, the conformation of *Pni*DAH7PS$^{\Delta 5AA}$ (*Pni*DAH7PS$_{rxn}^{\Delta 5AA}$) displayed a considerable increase in the protein size compared with that for *Pni*DAH7PS$_{PM}^{\Delta 5AA}$ (Table 3). The flexibility of *Pni*DAH7PSΔ5AA rxn remained high, as demonstrated by the Kratky and Porod–Debye plots (Fig. 6, *K* and *L*). Docking the homology models of DAH7PS barrel and loop-truncated CM dimer into the envelopes derived from the SAXS data of *Pni*DAH7PS$^{\Delta 5AA}$, *Pni*DAH7PS$_{PM}^{\Delta 5AA}$, and *Pni*DAH7PS$_{rxn}^{\Delta 5AA}$, all generate reasonable fits respectively with χ^2 values of 2.3, 0.9, and 1.8 (Fig. S3). Therefore, the increased flexibility is unlikely to be the result of disruption to the tertiary structure of either DAH7PS or CM domain. Overall, the truncated variant appears to respond differently from the wild-type enzyme to the presence of either PEP/Mn^{2+} or PEP/Mn^{2+}/E4P and maintains high flexibility under all of the conditions. These observations imply that the loop truncation likely weakens DAH7PS-CM interdomain interactions, which in turn interferes with the catalytic properties of *Pni*DAH7PS$^{\Delta 5AA}$.

Prephenate restricts the conformational change of Pni*DAH7PS and disrupts the catalytic cycle of DAH7PS reaction*

Previous studies only demonstrated the inhibitory effect of prephenate on *Pni*DAH7PS (15). Here we conducted kinetic assays for the DAH7PS activity in the presence of prephenate and observed higher K_m values for both PEP and E4P and a reduced k_{cat}, which led to the substantial reduction in specificity constant (Table 4).

We previously reported that upon the binding of prephenate, the conformational distribution of ligand-free *Pni*DAH7PS shifts toward a more compact and rigid average structure (15). This prephenate-bound conformation is more compact than that of *Pni*DAH7PS observed in the presence of either PEP/Mn^{2+} or PEP/Mn^{2+}/E4P, with an R_g value of 33 Å (Table 5). To further probe the effect of prephenate on the conformational variations of *Pni*DAH7PS associated with the occupancy of the DAH7PS active site, SAXS data for *Pni*DAH7PS was collected in the presence of both prephenate and combinations of DAH7PS active site ligands. Intriguingly, the distinct conformational populations observed for the prephenate-free *Pni*-DAH7PS (Table 1) are no longer apparent for the prephenate bound enzymes (Table 5 and Fig. 7). When prephenate is present, *Pni*DAH7PS maintains the compact and rigid conformations under different combinations of DAH7PS substrates (Table 5 and Fig. 7). This observation implies that prephenate binding not only shifts the conformational distribution of *Pni*-DAH7PS but also restricts the redistribution of conformations associated with the occupation of the DAH7PS active site.

As a comparison, the allostery of *Pni*DAH7PS$^{\Delta 5AA}$ by prephenate was investigated. Kinetic assays confirmed that *Pni*-DAH7PS$^{\Delta 5AA}$ is inhibited by prephenate as well. On the basis of the remarkable disruption of the substrate-binding of *Pni*-DAH7PS resulted by the loop truncation, the presence of prephenate further impairs the apparent affinities of *Pni*-DAH7PS$^{\Delta 5AA}$ for its substrates slightly (Table 4). As well, the turnover number of *Pni*DAH7PS$^{\Delta 5AA}$ is reduced in the

Table 3
SAXS parameters of ligand-free *Pni*DAH7PS$^{\Delta 5AA}$, *Pni*DAH7PS$_{PM}^{\Delta 5AA}$, and *Pni*DAH7PS$_{rxn}^{\Delta 5AA}$

	Ligand present		
	Ligand-free	PEP/Mn^{2+}	PEP/Mn^{2+}/E4P
Guinier analysis			
R_g (Å)	45.6± 0.8	39.9 ± 1.0	42.3± 1.7
I(0) (cm^{-1})	0.08 ± 0.00	0.07 ± 0.00	0.08 ± 0.00
Correlation coefficient, R^2	0.99	0.99	0.99
Pairwise distribution analysis			
R_g (Å)	46.1± 0.6	41.1± 0.5	43.4 ± 0.4
I(0) (cm^{-1})	0.08 ± 0.00	0.07 ± 0.00	0.08 ± 0.00
D_{max} (Å)	150.5	140.1	146.5
V_p (nm^3)	175	128	143
MM_{porod}			
MM (kDa)	103	75	84
Number of subunits	2	2	2

Abbreviations: MM_{porod}, molecular mass estimated from Porod volume; V_p, Porod volume.
The uncertainties represent standard deviations estimated by the error propagation from the experimental data.

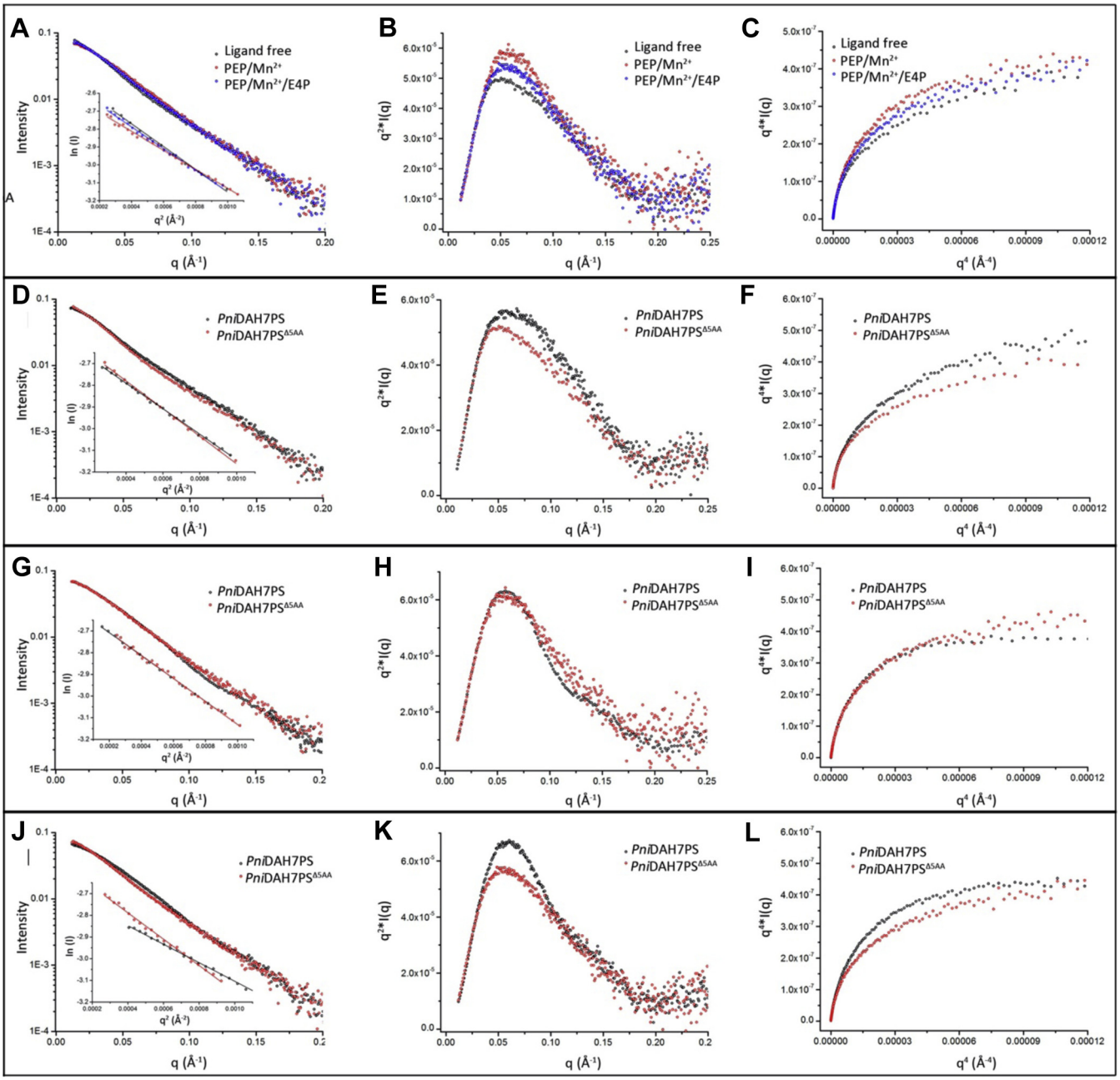

Figure 6. The analysis of the SAXS data for *Pni*DAH7PS$^{\Delta 5AA}$, and the comparison between the conformational changes of *Pni*DAH7PS$^{\Delta 5AA}$ and *Pni*DAH7PS resulted from the addition of either PEP/Mn^{2+} or PEP/Mn^{2+}/E4P. The *first panel* shows the SAXS profiles (*A*) and Kratky and Porod–Debye plots (*B* and *C*) of ligand-free *Pni*DAH7PS$^{\Delta 5AA}$ (*black*), *Pni*DAH7PS$^{\Delta 5AA}_{PM}$ (*red*), and *Pni*DAH7PS$^{\Delta 5AA}_{rxn}$ (*blue*) respectively. The *second panel* compares the SAXS profiles (*D*), the Kratky and Porod–Debye plots (*E* and *F*) of ligand-free *Pni*DAH7PS$^{\Delta 5AA}$ (*red*) with that of ligand-free *Pni*DAH7PS (*black*). The *third panel* compares the SAXS profiles (*G*), the Kratky and Porod–Debye plots (*H* and *I*) of *Pni*DAH7PS$^{\Delta 5AA}_{PM}$ (*red*) with that of *Pni*DAH7PS$_{PM}$ (*black*). The *fourth panel* compares the SAXS profiles (*J*), the Kratky and Porod–Debye plots (*K* and *L*) of *Pni*DAH7PS$^{\Delta 5AA}_{rxn}$ (*red*) with that of *Pni*DAH7PS$_{rxn}$ (*black*).

Table 4
Kinetic parameters for the DAH7PS activity of *Pni*DAH7PS in either the absence or the presence of 100 μM prephenate

Enzyme	K_M^{PEP} (μM)	K_M^{E4P} (μM)	k_{cat} (s^{-1})	k_{cat}/K_M^{PEP} ($\mu M^{-1}\cdot s^{-1}$)	k_{cat}/K_M^{E4P} ($\mu M^{-1}\cdot s^{-1}$)
Ligand-free *Pni*DAH7PS (15)	41 ± 4	58 ± 6	16.8 ± 0.5	0.41	0.29
Prephenate-*Pni*DAH7PS	102 ± 34	366 ± 51	4.8 ± 0.5	4.7×10^{-2}	1.3×10^{-2}
*Pni*DAH7PS$^{\Delta 5AA}$	212 ± 51	556 ± 77	11 ± 1	4.7×10^{-2}	1.8×10^{-2}
Prephenate-*Pni*DAH7PS$^{\Delta 5AA}$	228 ± 69	606 ± 90	7.2 ± 0.6	3.2×10^{-2}	1.1×10^{-2}

The Michaelis constants for the DAH7PS activity were obtained via fitting kinetic data to the equation of Alberty (as described in the Experimental procedures section). The uncertainty values represent the SD from triplicate measurements.

Table 5
SAXS parameters of ligand-free *Pni*DAH7PS and *Pni*DAH7PS in the presence of PEP/Mn^{2+} or PEP/Mn^{2+}/E4P, under the effect of prephenate

	Ligand present		
	Prephenate	prephenate & PEP/Mn^{2+}	prephenate & PEP/Mn^{2+}/E4P
Guinier analysis			
R_g (Å)	32.7 ± 0.3	29.7 ± 0.2	30.7 ± 0.5
$I(0)$ (cm^{-1})	0.06 ± 0.00	0.06 ± 0.00	0.06 ± 0.00
Correlation coefficient, R^2	0.99	0.99	0.99
Pairwise distribution analysis			
R_g (Å)	33.0 ± 0.2	29.5 ± 0.4	30.5 ± 0.1
$I(0)$ (cm^{-1})	0.06 ± 0.00	0.06 ± 0.00	0.06 ± 0.00
D_{max} (Å)	113.0	87.0	93.4
V_p (nm^3)	114	109	108
MM_{porod}			
MM (kDa)	67	64	63
Number of subunits	2	2	2

Abbreviations: MM_{porod}, molecular mass estimated from Porod volume; V_p, Porod volume
The uncertainties represent standard deviations estimated by the error propagation from the experimental data.

presence of prephenate, but nonetheless this is faster than that shown by prephenate-bound *Pni*DAH7PS (Table 4). In general, with the shortened $loop_{C320\text{-}F333}$, *Pni*DAH7PS shows diminished sensitivity to the inhibitory effect of prephenate. SAXS data collected for *Pni*DAH7PS$^{\Delta 5AA}$ in the presence of prephenate indicates a more compact and rigid conformation than that of ligand-free *Pni*DAH7PS$^{\Delta 5AA}$ (Fig. S4). However, compared with the structure of prephenate-bound *Pni*DAH7PS, this prephenate-bound *Pni*DAH7PS$^{\Delta 5AA}$ displays more flexibility (Table S1 and Fig. S4).

Discussion

Our previous studies of *Pni*DAH7PS uncovered an unexpected dependency between the catalytic functions of the CM and DAH7PS domains in this C-terminal CM-linked DAH7PS (15). Structural studies demonstrated that this bifunctional protein is homodimeric. In contrast to other DAH7PS enzymes, the DAH7PS domains do not directly associate and the dimer interface in *Pni*DAH7PS is only formed between the two CM domains. Therefore, the interdependency of activities between DAH7PS and CM domains in *Pni*DAH7PS can only be accounted for by direct and DAH7PS-CM interdomain interactions. In this study, we explore the conformational plasticity of this bifunctional enzyme more fully and examine the impact of substrate binding at the DAH7PS active site on the overall structure and CM catalytic function.

Scattering data demonstrates that *Pni*DAH7PS is highly flexible and does not adopt a single dominant conformation during DAH7PS catalysis. Two distinct conformational populations of the enzyme, with different DAH7PS-CM interactions, were identified, specific to the presence of either PEP/Mn^{2+} or PEP/Mn^{2+}/E4P. The most compact structure of *Pni*DAH7PS was observed when PEP/Mn^{2+}/E4P were present, namely when the DAH7PS-catalyzed reaction was ongoing. Intriguingly under these conditions, CM activity was substantially enhanced (Fig. 2, *A*). Therefore, we propose that the catalytic cycle of DAH7PS is intimately linked to a series of variations in DAH7PS-CM interaction, in which catalytic steps and interdomain rearrangements occur in concert to improve and fine-tune DAH7PS and CM enzymatic functions (Fig. 8).

Based on sequence alignments and rigid body models for *Pni*DAH7PS (Fig. 9), an extended loop within CM domain,

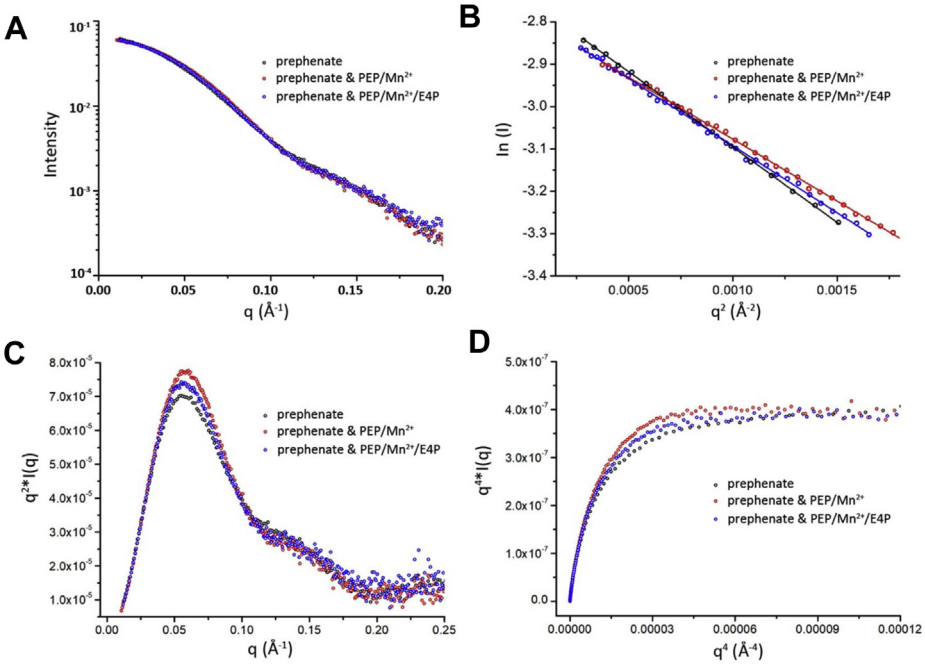

Figure 7. The analysis of SAXS profiles shows the structural effect of prephenate on ligand-free *Pni*DAH7PS (*black*) and *Pni*DAH7PS in the presence of PEP/Mn^{2+} (*red*) or PEP/Mn^{2+}/E4P (*blue*). *A*, SAXS profiles (log $I(q)$ *versus* q). *B*, Guinier analysis (ln $I(q)$ *versus* q^2). *C*, Kratky plot (q^2*I(q) *versus* q). *D*, Porod–Debye plot (q^4*$I(q)$ *versus* q^4) limited to the range of the SAXS data for which the Guinier linearity was observed.

$Loop_{C320\text{-}F333}$, which is present in this fused DAH7PS-CM yet not in other CM types, has been identified as a potential structural component that may facilitate communication to the DAH7PS domain. The functional importance of this loop was confirmed by truncation of this loop, which disrupted both the DAH7PS catalytic activity and the reaction-correlated conformational changes. Considering the complex allosteric behaviors associated with the substantial conformational changes displayed by *Pni*DAH7PS, the flexible properties of the long loop may be advantageous in assisting structural and functional variations (5).

Allosteric control of DAH7PS is an important strategy for metabolic regulation. Prephenate binding at the CM domain allosterically inhibits the DAH7PS activity, and the compact structure of the *Pni*DAH7PS dimer in the presence of prephenate has been previously reported (15). Here, we observe that prephenate binding restricts the structural flexibilities of *Pni*DAH7PS associated with binding of the DAH7PS substrates. In addition, following the truncation of $Loop_{C320\text{-}F333}$, *Pni*DAH7PS becomes less sensitive to the inhibitory effect of prephenate, which is associated with a more flexible prephenate-bound structure. Based on these observations, it is hypothesized that the flexibility restrictions of *Pni*DAH7PS by prephenate could attenuate the dynamic DAH7PS-CM interactions and likely disrupt the DAH7PS catalytic cycle.

Assembly of multiple enzymes in metabolic pathways is commonly found to enhance overall specificity constant *via* colocalizing or directly channeling multiple active sites that catalyze consecutive chemical reactions (34–36). In addition, in some bienzyme assemblies, one functional domain/unit can play a role as the regulatory element, delivering an allosteric effect derived from its ligand binding to the other enzymatic moiety (11, 22). In contrast, the bifunctional system of *Pni*DAH7PS joins together two nonconsecutive enzymatic moieties; a fusion that does not serve for purpose of substrate sequestration or channeling. Furthermore, *Pni*DAH7PS displays a sophisticated interconnection between its DAH7PS and CM domains, which distinguishes it from other well-studied bifunctional enzymatic systems. Specifically, in addition to the allosteric inhibition of DAH7PS by prephenate, the upregulation of CM activity in the presence of $PEP/Mn^{2+}/E4P$ delivers allosteric activation of CM mediated by the DAH7PS domain, revealing reciprocal allostery along with catalytic dependency.

This reciprocal allostery and functional interdependency of *Pni*DAH7PS provide complex feedback and feedforward response (Fig. 10). Moreover, the cooperation between the feedforward activation of CM and the feedback inhibition on DAH7PS activity by prephenate allows for bidirectional regulation between the initiation and a branch point of the shikimate pathway, which enables *Pni*DAH7PS to more precisely sense both the input signals of carbon resources (PEP and E4P) and tune the output of the crucial intermediate of the shikimate pathway. Whether such complex

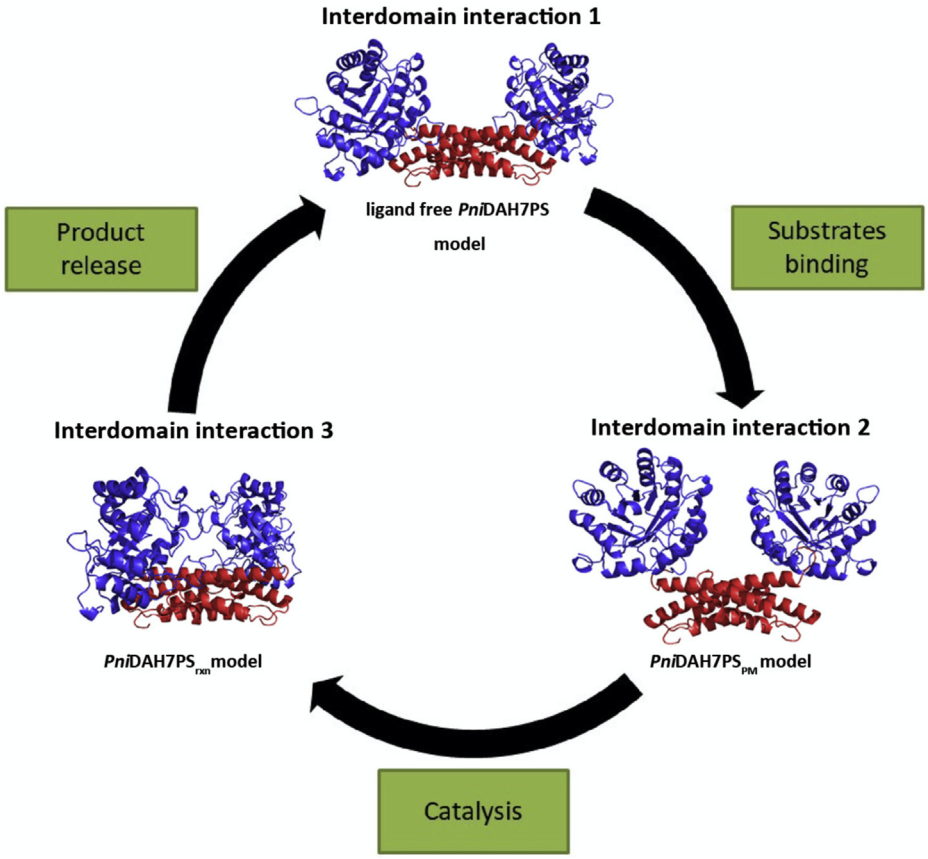

Figure 8. Schematic showing the hypothesized cycle of interdomain interaction of *Pni*DAH7PS throughout the DAH7PS-catalyzed reaction.

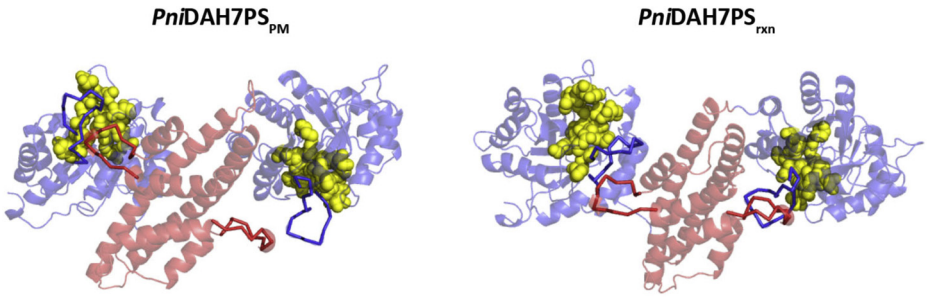

Figure 9. Rigid body models of *Pni*DAH7PS show the interaction between the DAH7PS (*blue cartoon*) and CM (*red cartoon*) domains respectively in the presence of PEP/Mn^{2+} (*left*) and PEP/Mn^{2+}/E4P (*right*). The *red* and *blue ribbon diagrams* respectively indicate $Loop_{C320\text{-}F333}$ and loop β6-α6 of DAH7PS domain that is involved in the formation of the DAH7PS active site. The *yellow spheres* represent the active site of DAH7PS.

bidirectional regulation embedded in a single multienzyme assembly is present in other biosynthetic pathways remain to be explored.

Experimental procedures

Bacterial strains, plasmids, media, and growth conditions

The detailed methods for cloning, expressing, and purifying the wild-type *Pni*DAH7PS have been described previously (15). Briefly, the *Pni*DAH7PS gene was cloned into pET28a vector and expressed in *Escherichia coli* BL21 (DE3) pBB540/pBB542 cells using IPTG induction. Following sonication cell lysis, the overexpressed protein was purified using HiTrap TALON crude column (GE Healthcare). The eluate from Talon column was treated by Tobacco Etch Virus (TEV) protease for the removal of His tag and subsequently subjected to Superdex S200 26/60 column (GE Healthcare) for further purification. The purified protein was concentrated and stored at −80 °C.

The generation of PniDAH7PS$^{\Delta 5AA}$ truncated variant

The removal of the C327-T331 segment from the CM domain of *Pni*DAH7PS was performed using a QuikChange II Site-Directed Mutagenesis Kit (Stratagene). The pET28a-*Pni*-DAH7PS plasmid was used as the template, and the deletion was generated using the primers as follows:

Forward primer: 5′-AAAATGTGCACGTCAGGCAAA TGCAAAATTTGCAGCACGTATTCTGGAAA-3′
Reverse primer: 5′-TTTCCAGAATACGTGCTGCAAA TTTTGCATTTGCCTGACGTGCACATTTT-3′

PCR products were digested by *Dpn*I at 37 °C to remove the parental plasmids before they were transformed into TOP10 cells and purified. After being sequenced, plasmids with the correct deletion were transformed into *E. coli* BL21 (DE3) cells. Protein expression and purification were carried out using the same methods for obtaining the purified wild-type *Pni*DAH7PS.

Kinetic characterization

A modified continuous assay for the spectrophotometric analysis of either DAH7PS or CM enzymatic activity (37) was employed to determine the kinetic parameters of the wild-type enzyme and *Pni*DAH7PS$^{\Delta 5AA}$. In the standard assay, a 50 mM Bis-Tris propane (BTP) buffer (pH 7.4) was applied for either DAH7PS or CM catalysed reaction. Enzymatic reactions were carried out in 1 ml quartz cuvettes with 1 cm path length at 35

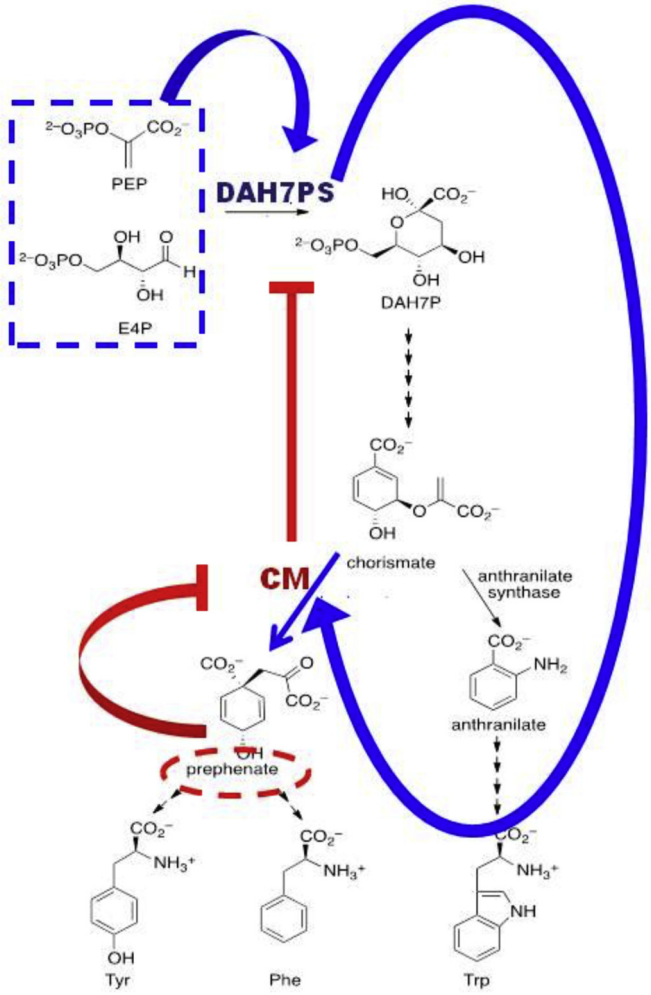

Figure 10. Schematic representation of the proposed bidirectional regulation mediated by *Pni*DAH7PS in the shikimate pathway. The *blue point arrows* represent the DAH7PS-catalyzed reaction (highlighted by *blue dash rectangle*) induced feedforward activation of CM activity, promoting the conversion of chorismate to prephenate; the *red blunt arrows* illustrate the feedback inhibition of the DAH7PS activity by prephenate (highlighted by *red dash oval*) via the CM domain.

°C, and the reaction rates were monitored by the disappearance of the substrate PEP at 232 nm (2800 M^{-1} cm^{-1}) or chorismate at 274 nm (ϵ = 2630 M^{-1} cm^{-1}) for the DAH7PS and CM activities, respectively (37, 38). To avoid influence from unexpected metal ions, buffer and all reactions components were prepared using the ultrapure water pretreated by chelating ion exchange resin, Chelex 100 (BioRad). Substrates E4P, chorismate, and inhibitor prephenate were supplied from Sigma-Aldrich; PEP was obtained from Alfa Aesar.

Determination of the allosteric regulation of CM activity

To detect if there would be any detectable change at 274 nm due to the additions of the components of DAH7PS reaction rather than CM-catalyzed reaction, the absorption of 500 μM PEP, 500 μM E4P, 100 μM $MnSO_4$, or 500 μM DAH7P at this wavelength was checked in either the presence or absence of chorismate or *Pni*DAH7PS. The results did not exhibit any significant change in absorption. To further confirm this, a DAH7PS-catalyzed reaction was initiated and the absorbance at 274 nm was monitored, and no significant absorption was observed over time.

The determination of the effects of Mn^{2+} and the substrates of DAH7PS-catalyzed reaction on CM activity was carried out with 7.3 × 10^{-2} μM *Pni*DAH7PS using 100 μM chorismate, respectively, in the presence of 100 μM $MnSO_4$, 500 μM PEP, and 500 μM E4P alone or combinations of $MnSO_4$ (100 μM)/PEP (500 μM), $MnSO_4$ (100 μM)/E4P (500 μM), and PEP (500 μM)/E4P (500 μM). The effect of the presence of the products of DAH7PS reaction on CM activity was examined in the presence of DAH7P/sodium phosphate combination with a concentration of either 500 μM or 2.5 mM for each product. It was observed that the products at a concentration of 2.5 mM each are inhibitory of DAH7PS activity (Fig. S1). As well, the allosteric regulation of CM activity was detected as the DAH7PS-catalyzed reaction is proceeding. In this assay a DAH7PS catalyzed reaction, containing 500 μM PEP, 100 μM $MnSO_4$, and 500 μM E4P, was started by either 7.3 × 10^{-2} μM *Pni*DAH7PS or *Gsp*DAH7PS. Under these conditions, the DAH7PS reaction is expected to take approximately 8 min until substrates are exhausted. Following 5 s incubation of the DAH7PS reaction, the CM reaction was initiated by the addition of 100 μM chorismate to determine the CM activity. In total, 5 s incubation makes sure that the DAH7PS-catalyzed reaction is in the linear steady-state phase.

Determination of the kinetic characteristics of PniDAH7PS$^{\Delta 5AA}$

The assays for determining the kinetic parameters of the DAH7PS activity for *Pni*DAH7PS$^{\Delta 5AA}$ contained 100 μM $MnSO_4$, 0.26 μM enzyme in the BTP buffer. All reactions were initiated by the addition of E4P. Because of the high apparent K_M for E4P of *Pni*DAH7PS$^{\Delta 5AA}$ and the dimerization of E4P at high concentrations (39), the equation of Alberty was employed to calculate the kinetic parameters. In this assay, the rate of consumption of PEP was measured at different fixed concentrations of PEP (167, 267 and 533 μM respectively) as E4P concentration was varied (63–221 μM). The data was fitted to the equation of Alberty (40):

$$\upsilon_0 = \frac{V_{max}[A][B]}{K_M^B[A] + K_M^A + [A][B] + K_S^A K_M^B}$$

Where V_{max} is the maximum possible reaction rate υ_0; [A] is the concentration of the variable substrate (E4P), and [B] is the fixed concentration of the other substrate (PEP) for each Michaelis–Menten kinetic measurement; $K_M{}^B$ ($K_M{}^A$) is the concentration of substrate B (A), which gives ½V_{max} when substrate A (B) is saturating; $K_S{}^A$ is the disassociation constant of substrate A.

The reactions for determining the kinetic characteristics for the CM domain contained 9.4 × 10^{-2} μM enzyme in 50 mM BTP buffer (pH 7.4) and initiated by the addition of chorismate with a series of concentrations (22–441 μM).

Determination of the inhibitory effect of prephenate on the wild-type PniDAH7PS and PniDAH7PS$^{\Delta 5AA}$

The conditions and procedures for the kinetic assays for determining the *Pni*DAH7PS$^{\Delta 5AA}$ kinetic properties were used to inspect the kinetic characterization of the DAH7PS activity of *Pni*DAH7PS or *Pni*DAH7PS$^{\Delta 5AA}$ under the effect of prephenate. The only modification to suit the purpose is that all reactions were preincubated with prephenate at a saturating concentration of 100 μM (15) before being initiated by the addition of E4P.

SAXS

SAXS measurements were carried out using the Australian Synchrotron (41–43) SAXS/WAXS beamline equipped with a Pilatus detector (1 M, 170 × 170 mm, effective pixel size, 172 × 172 mm). The applied wavelength of X-ray was 1.0332 Å, and a sample detector, at a distance of 1.6 m from the sample, recorded scattered X-rays intensities covering the q range of 0.0015–3.0 $Å^{-1}$. Either wild-type *Pni*DAH7PS or *Pni*DAH7PS$^{\Delta 5AA}$ was eluted from a SEC column (Superdex increase 200 5/150) using SEC buffer (10 mM BTP, pH 7.4, 150 mM NaCl and 3% (v/v) glycerol) and the buffers containing various additives of interest as listed in Table 6. The eluted sample was passed into a 1.0 mm thin-walled glass capillary where the sample was detected using X-rays at 25 °C at 1 s intervals. The raw scattering data was processed using Scatterbrain, developed at the Australian Synchrotron, for data reduction and buffer subtraction. Processed data were plotted as $I(q)$ *versus* q (q = (4πsinθ)/λ, 2θ is the scattering angle) and analyzed using Primus (44).

All data sets for structural analysis were recorded with ∼400 data points over the range 0.005 ≤ q ≤ 0.35 $Å^{-1}$, which took ∼400 s. A single symmetric scattering peak over ∼120 frames was observed only at the middle part of each data set. In the experiment to record the data in the presence of PEP/Mn^{2+}/E4P, the amounts of PEP and E4P (at 500 μM each) present in the buffer were sufficient to be present in a timeframe that exceeded this sample collection time, taking into account the

Table 6
Additives in SEC buffers for SAXS examinations of *Pni*DAH7PS or *Pni*DAH7PS$^{\Delta 5AA}$

Protein sample	Additives in SEC buffers
*Pni*DAH7PS or *Pni*DAH7PS$^{\Delta 5AA}$	500 μM PEP, 100 μM $MnSO_4$ 500 μM PEP, 100 μM $MnSO_4$, 500 μM E4P
*Pni*DAH7PS	500 μM PEP, 100 μM $MnSO_4$, 100 μM prephenate 500 μM PEP, 100 μM $MnSO_4$, 500 μM E4P, 100 μM prephenate

two- to fourfold dilution of the enzyme through the column. To confirm conformational homogeneity, three different groups of data respectively covering the maximum scattering intensity and either side of the scattering maximum were summed and compared. The same scattering profile was observed across each scattering peak. The radius of gyration (R_g) of the protein particle was evaluated from Guinier plots ($\ln I(q)$ *versus* q^2) of scattering data. In addition, the linear Guinier plot in the q range of $q \geq 1.3/R_g$ was a crucial indicator of the monodispersity of samples. The Porod volume (V_p) and the maximum distance (D_{max}) of the protein particle were evaluated respectively from the Porod plot and the pair-distance distribution ($P(r)$) function obtained *via* Fourier transformation. MM_{porod} was obtained by dividing the Porod volumes by 1.7.

Homology and rigid body modeling

Homology modeling of monomeric *Pni*DAH7PS^{D} and dimeric *Pni*DAH7PS^{CM} was performed by Modeler using *Pfu*DAH7PS (45) and *Pfu*CM (46) as template structures, respectively (47). Then, the two resultant homology models were connected together as a full-length monomeric unit (*Pni*DAH7PS-CM) containing an undefined linker using the software PRE_BUNCH (48). Subsequently, two *Pni*DAH7PS-CM monomeric models were docked into the SAXS *ab initio* envelope of ligand-free *Pni*DAH7PS, *Pni*DAH7PS$_{PM}$, and *Pni*DAH7PS$_{rxn}$ to generate a rigid body model using BUNCH, constrained by twofold symmetry and distance information of the contacting residues obtained from the homology model of the *Pni*DAH7PS^{CM} dimer (Table 7).

Circular dichroism

The CD spectra were recorded on a Chirascan-Plus CD spectrometer (Applied Photophysics). Samples were prepared at ~0.03 mg/ml in 10 mM potassium phosphate buffer (pH 7.4) and measured in a 3 ml quartz cuvette with 1 cm pathlength. Wavelength scans were carried out from 260 to 190 nm, with 1 s response, 1 nm bandwidth at 25 °C.

Table 7
Contact information for rigid body modeling of *Pni*DAH7PS using BUNCH

Residue of chain 1	Residue of chain 2	Distance between C_α atoms (Å)
R272	Q309	12.0
D276	R312	11.0
D279	R289	8.5
R289	D279	8.5
R312	D276	11.0
K319	D276	10.0
I340	I341	10.0
I341	I340	10.0

Data availability

All data are given in the main manuscript or supporting information.

Supporting information—This article contains supporting information.

Acknowledgments—Data were collected at the SAXS beamlines of the Australian Synchrotron (41, 42) with access provided by the New Zealand Synchrotron Group. Dr Wanting Jiao (Ferrier Research Institute, Victoria University of Wellington) reviewed this manuscript and provided valuable comments. This work was supported by funding from the New Zealand Marsden Fund (VUW1426) administered by the Royal Society of New Zealand.

Author contributions—Y. B. and E. J. P. conceptualization; Y. B. data curation; Y. B. formal analysis; E. J. P. funding acquisition; Y. B. investigation; Y. B. and E. J. P. methodology; E. J. P. project administration; E. J. P. supervision; Y. B. writing–original draft; E. J. P. writing–review and editing.

Funding and additional information—Marsden Fund VUW1426.

Conflict of interest—The authors declare that they have no conflicts of interest with the contents of this article.

Abbreviations—The abbreviations used are: *Ape*CM, monofunctional CM from *Aeropyrum pernix*; CM, chorismate mutase; DAH7PS, 3-deoxy-D-*arabino*-heptulosonate 7-phosphate synthase; E4P, erythrose 4-phosphate; *Gsp*DAH7PS, N-terminal CM-linked DAH7PS from *Geobacillus sp.*; *Mtu*DAH7PS-CM, DAH7PS-CM complex from *Mycobacterium tuberculosis*; PEP, phosphoenolpyruvate; *Pfu*CM, monofunctional CM from *Pyrococcus furiosus*; *Pgi*DAH7PS, C-terminal CM-linked DAH7PS from *Porphyromonas gingivalis*; *Pgi*DAH7PS^{CM}, CM domain of *Pgi*DAH7PS; *Pni*DAH7PS, C-terminal CM-linked DAH7PS from *Prevotella nigrescens* DAH7PS; *Pni*DAH7PS$_{PM}$, PEP/Mn^{2+}-bound *Pni*DAH7PS; *Pni*-DAH7PS^{CM}, CM domain of *Pni*DAH7PS; *Pni*DAH7PS$^{\Delta 5AA}$, truncated *Pni*DAH7PS variant with removal of C327-T331 residues; *Pni*DAH7PS$^{\Delta 5AA}_{PM}$, PEP/Mn^{2+}-bound *Pni*DAH7PS$^{\Delta 5AA}$; *Pni*DAH7PS$^{\Delta 5AA}_{rxn}$, *Pni*DAH7PS$^{\Delta 5AA}$ in the presence of PEP/Mn^{2+}/E4P; *Pni*DAH7PS^{D}, DAH7PS domain of *Pni*DAH7PS; *Pni*DAH7PS$_{rxn}$, *Pni*DAH7PS in the presence of PEP/Mn^{2+}/E4P; SAXS, small-angle X-ray Scattering; SEC, size-exclusion chromatography.

References

1. Goodey, N. M., and Benkovic, S. J. (2008) Allosteric regulation and catalysis emerge via a common route. *Nat. Chem. Biol.* **4**, 474–482
2. Laskowski, R. A., Gerick, F., and Thornton, J. M. (2009) The structural basis of allosteric regulation in proteins. *FEBS Lett.* **583**, 1692–1698
3. Huang, Q., Li, M., Lai, L., and Liu, Z. (2020) Allostery of multidomain proteins with disordered linkers. *Curr. Opin. Struct. Biol.* **62**, 175–182
4. Xie, J., and Lai, L. (2020) Protein topology and allostery. *Curr. Opin. Struct. Biol.* **62**, 158–165
5. Papaleo, E., Saladino, G., Lambrughi, M., Lindorff-Larsen, K., Gervasio, F. L., and Nussinov, R. (2016) The role of protein loops and linkers in conformational dynamics and allostery. *Chem. Rev.* **116**, 6391–6423

6. Jiao, W., Lang, E. J., Bai, Y., Fan, Y., and Parker, E. J. (2020) Diverse allosteric componentry and mechanisms control entry into aromatic metabolite biosynthesis. *Curr. Opin. Struct. Biol.* **65**, 159–167
7. Lang, E. J., Cross, P. J., Mittelstadt, G., Jameson, G. B., and Parker, E. J. (2014) Allosteric ACTion: The varied ACT domains regulating enzymes of amino-acid metabolism. *Curr. Opin. Struct. Biol.* **29**, 102–111
8. Light, S. H., and Anderson, W. F. (2013) The diversity of allosteric controls at the gateway to aromatic amino acid biosynthesis. *Protein Sci.* **22**, 395–404
9. Shumilin, I. A., Bauerle, R., Wu, J., Woodard, R. W., and Kretsinger, R. H. (2004) Crystal structure of the reaction complex of 3-deoxy-D-*arabino*-heptulosonate-7-phosphate synthase from *Thermotoga maritima* refines the catalytic mechanism and indicates a new mechanism of allosteric regulation. *J. Mol. Biol.* **341**, 455–466
10. Wu, J., and Woodard, R. W. (2006) New insights into the evolutionary links relating to the 3-deoxy-D-*arabino*-heptulosonate 7-phosphate synthase subfamilies. *J. Biol. Chem.* **281**, 4042–4048
11. Nazmi, A. R., Lang, E. J. M., Bai, Y., Allison, T. M., Othman, M. H., Panjikar, S., Arcus, V. L., and Parker, E. J. (2016) Interdomain Conformational Changes Provide Allosteric Regulation en Route to Chorismate. *J. Biol. Chem.* **291**, 21836–21847
12. Cross, P. J., Allison, T. M., Dobson, R. C., Jameson, G. B., and Parker, E. J. (2013) Engineering allosteric control to an unregulated enzyme by transfer of a regulatory domain. *Proc. Natl. Acad. Sci. U. S. A.* **110**, 2111–2116
13. Fan, Y., Cross, P. J., Jameson, G. B., and Parker, E. J. (2018) Exploring modular allostery via interchangeable regulatory domains. *Proc. Natl. Acad. Sci. U. S. A.* **115**, 3006–3011
14. Furdui, C., Zhou, L., Woodard, R. W., and Anderson, K. S. (2004) Insights into the mechanism of 3-deoxy-D-*arabino*-heptulosonate 7-phosphate synthase (Phe) from *Escherichia coli* using a transient kinetic analysis. *J. Biol. Chem.* **279**, 45618–45625
15. Bai, Y., Lang, E. J. M., Nazmi, A. R., and Parker, E. J. (2019) Domain cross-talk within a bifunctional enzyme provides catalytic and allosteric functionality in the biosynthesis of aromatic amino acids. *J. Biol. Chem.* **294**, 4828–4842
16. Zhou, L., Wu, J., Vijayalakshmi, J., Shumilin, I. A., Bauerle, R., Kretsinger, R. H., and Woodard, R. W. (2012) Structure and characterization of the 3-deoxy-D-*arabino*-heptulosonate 7-phosphate synthase from *Aeropyrum pernix*. *Bioorg. Chem.* **40**, 79–86
17. Webby, C. J., Baker, H. M., Lott, J. S., Baker, E. N., and Parker, E. J. (2005) The structure of 3-deoxy-D-*arabino*-heptulosonate 7-phosphate synthase from *Mycobacterium tuberculosis* reveals a common catalytic scaffold and ancestry for type I and type II enzymes. *J. Mol. Biol.* **354**, 927–939
18. Cross, P. J., Dobson, R. C., Patchett, M. L., and Parker, E. J. (2011) Tyrosine latching of a regulatory gate affords allosteric control of aromatic amino acid biosynthesis. *J. Biol. Chem.* **286**, 10216–10224
19. Nazmi, A. R., Schofield, L. R., Dobson, R. C., Jameson, G. B., and Parker, E. J. (2014) Destabilization of the homotetrameric assembly of 3-deoxy-D-*arabino*-heptulosonate-7-phosphate synthase from the hyperthermophile *Pyrococcus furiosus* enhances enzymatic activity. *J. Mol. Biol.* **426**, 656–673
20. Cross, P. J., Heyes, L. C., Zhang, S., Nazmi, A. R., and Parker, E. J. (2016) The functional unit of *Neisseria meningitidis* 3-deoxy-D-*arabino*-heptulosonate 7-phosphate synthase is dimeric. *PLoS One* **11**, e0145187
21. Cross, P. J., Pietersma, A. L., Allison, T. M., Wilson-Coutts, S. M., Cochrane, F. C., and Parker, E. J. (2013) *Neisseria meningitidis* expresses a single 3-deoxy-D-*arabino*-heptulosonate 7-phosphate synthase that is inhibited primarily by phenylalanine. *Protein Sci.* **22**, 1087–1099
22. Light, S. H., Halavaty, A. S., Minasov, G., Shuvalova, L., and Anderson, W. F. (2012) Structural analysis of a 3-deoxy-D-*arabino*-heptulosonate 7-phosphate synthase with an N-terminal chorismate mutase-like regulatory domain. *Protein Sci.* **21**, 887–895
23. MacBeath, G., Kast, P., and Hilvert, D. (1998) A small, thermostable, and monofunctional chorismate mutase from the archaeon *Methanococcus jannaschii*. *Biochemistry* **37**, 10062–10073
24. Lee, A. Y., Stewart, J. D., Clardy, J., and Ganem, B. (1995) New insight into the catalytic mechanism of chorismate mutases from structural studies. *Chem. Biol.* **2**, 195–203
25. Lee, A. Y., Angrew Karplus, P., Ganem, B., and Clardy, J. (1995) Atomic structure of the buried catalytic pocket of *Escherichia coli* chorismate mutase. *J. Am. Chem. Soc.* **117**, 3627–3628
26. Helmstaedt, K., Heinrich, G., Merkl, R., and Braus, G. H. (2004) Chorismate mutase of *Thermus thermophilus* is a monofunctional AroH class enzyme inhibited by tyrosine. *Arch. Microbiol.* **181**, 195–203
27. Mistry, J., Chuguransky, S., Williams, L., Qureshi, M., Salazar, G. A., Sonnhammer, E. L. L., Tosatto, S. C. E., Paladin, L., Raj, S., Richardson, L. J., Finn, R. D., and Bateman, A. (2021) Pfam: The protein families database in 2021. *Nucleic Acids Res.* **49**, D412–D419
28. Burschowsky, D., Thorbjornsrud, H. V., Heim, J. B., Fahrig-Kamarauskaite, J. R., Wurth-Roderer, K., Kast, P., and Krengel, U. (2018) Interenzyme allosteric regulation of chorismate mutase in *Corynebacterium glutamicum*: Structural basis of feedback activation by Trp. *Biochemistry* **57**, 557–573
29. Okvist, M., Sasso, S., Roderer, K., Kast, P., and Krengel, U. (2009) A novel noncovalent complex of chorismate mutase and DAHP synthase from *Mycobacterium tuberculosis*: Protein purification, crystallization and X-ray diffraction analysis. *Acta Crystallogr. F Struct. Biol. Cryst. Commun.* **65**, 1048–1052
30. Blackmore, N. J., Nazmi, A. R., Hutton, R. D., Webby, M. N., Baker, E. N., Jameson, G. B., and Parker, E. J. (2015) Complex formation between two biosynthetic enzymes modifies the allosteric regulatory properties of both: An example of molecular symbiosis. *J. Biol. Chem.* **290**, 18187–18198
31. Sasso, S., Okvist, M., Roderer, K., Gamper, M., Codoni, G., Krengel, U., and Kast, P. (2009) Structure and function of a complex between chorismate mutase and DAHP synthase: Efficiency boost for the junior partner. *EMBO J.* **28**, 2128–2142
32. Webby, C. J., Jiao, W., Hutton, R. D., Blackmore, N. J., Baker, H. M., Baker, E. N., Jameson, G. B., and Parker, E. J. (2010) Synergistic allostery, a sophisticated regulatory network for the control of aromatic amino acid biosynthesis in *Mycobacterium tuberculosis*. *J. Biol. Chem.* **285**, 30567–30576
33. Jiao, W., Hutton, R. D., Cross, P. J., Jameson, G. B., and Parker, E. J. (2012) Dynamic cross-talk among remote binding sites: The molecular basis for unusual synergistic allostery. *J. Mol. Biol.* **415**, 716–726
34. Hyde, C. C., Ahmed, S. A., Padlan, E. A., Miles, E. W., and Davies, D. R. (1988) Three-dimensional structure of the tryptophan synthase $\alpha_2\beta_2$ multienzyme complex from *Salmonella typhimurium*. *J. Biol. Chem.* **263**, 17857–17871
35. Singh, H., Arentson, B. W., Becker, D. F., and Tanner, J. J. (2014) Structures of the PutA peripheral membrane flavoenzyme reveal a dynamic substrate-channeling tunnel and the quinone-binding site. *Proc. Natl. Acad. Sci. U. S. A.* **111**, 3389–3394
36. Wilmanns, M., Priestle, J. P., Niermann, T., and Jansonius, J. N. (1992) Three-dimensional structure of the bifunctional enzyme phosphoribosylanthranilate isomerase: Indoleglycerolphosphate synthase from *Escherichia coli* refined at 2.0 Å resolution. *J. Mol. Biol.* **223**, 477–507
37. Schoner, R., and Herrmann, K. M. (1976) 3-deoxy-D-*arabino*-heptulosonate 7-phosphate synthase. Purification, properties, and kinetics of the tyrosine-sensitive isoenzyme from *Escherichia coli*. *J. Biol. Chem.* **251**, 5440–5447
38. Sasso, S., Ramakrishnan, C., Gamper, M., Hilvert, D., and Kast, P. (2005) Characterization of the secreted chorismate mutase from the pathogen *Mycobacterium tuberculosis*. *FEBS J.* **272**, 375–389
39. Blackmore, P. F., Williams, J. F., and MacLeod, J. K. (1976) Dimerization of erythrose 4-phosphate. *FEBS Lett.* **64**, 222–226
40. Palmer, T., and Bonner, P. L. (2007) *Enzymes: Biochemistry, Biotechnology, Clinical Chemistry*, Woodhead Publishing Limited, Cambridge, UK
41. Kirby, N., Boldeman, J., Gentle, I., and Cookson, D. (2007) Conceptual design of the small angle scattering beamline at the australian synchrotron. In *AIP Conference Proceedings*. American Institute of Physics publishing, Melville, NY
42. Kirby, N. M., Mudie, S. T., Hawley, A. M., Cookson, D. J., Mertens, H. D., Cowieson, N., and Samardzic-Boban, V. (2013) A low-background-

intensity focusing small-angle X-ray scattering undulator beamline. *J. Appl. Cryst.* **46**, 1670–1680
43. Ryan, T. M., Trewhella, J., Murphy, J. M., Keown, J. R., Casey, L., Pearce, F. G., Goldstone, D. C., Chen, K., Luo, Z., and Kobe, B. (2018) An optimized SEC-SAXS system enabling high X-ray dose for rapid SAXS assessment with correlated UV measurements for biomolecular structure analysis. *J. Appl. Cryst.* **51**, 97–111
44. Konarev, P. V., Volkov, V. V., Sokolova, A. V., Koch, M. H. J., and Svergun, D. I. (2003) *Primus*: A Windows PC-based system for small-angle scattering data analysis. *J. Appl. Cryst.* **36**, 1295–1296
45. Schofield, L. R., Anderson, B. F., Patchett, M. L., Norris, G. E., Jameson, G. B., and Parker, E. J. (2005) Substrate ambiguity and crystal structure of *Pyrococcus furiosus* 3-deoxy-D-*arabino*-heptulosonate-7-phosphate synthase: An ancestral 3-deoxyald-2-ulosonate-phosphate synthase? *Biochemistry* **44**, 11950–11962
46. Lee, D., Chen, L., Nguyen, D., Dillard, B.D., Tempel, W., Habel, J., Zhou, W., Chang, S.-H., Kelley, L.-L.C., Liu, Z.-J., Lin, D., Zhang, H., Praissman, J., Bridger, S., Eneh, J.C., *et al.* (2005) PDB ID: 1YBZ Conserved hypothetical protein from *Pyrococcus furiosus* Pfu-1581948-001. Protein Data Bank.
47. Sali, A., and Blundell, T. L. (1993) Comparative protein modelling by satisfaction of spatial restraints. *J. Mol. Biol.* **234**, 779–815
48. Petoukhov, M. V., and Svergun, D. I. (2005) Global rigid body modeling of macromolecular complexes against small-angle scattering data. *Biophys. J.* **89**, 1237–1250